Photoelectrochemistry at semiconductor/liquid interfaces triggered by electrochemiluminescence

Yiran Zhao, Jing Yu, Jean-Francois Bergamini, Yoan Léger, Neso Sojic, Gabriel Loget

Cell Reports
Physical Science

CellPress
OPEN ACCESS

Article

Photoelectrochemistry at semiconductor/liquid interfaces triggered by electrochemiluminescence

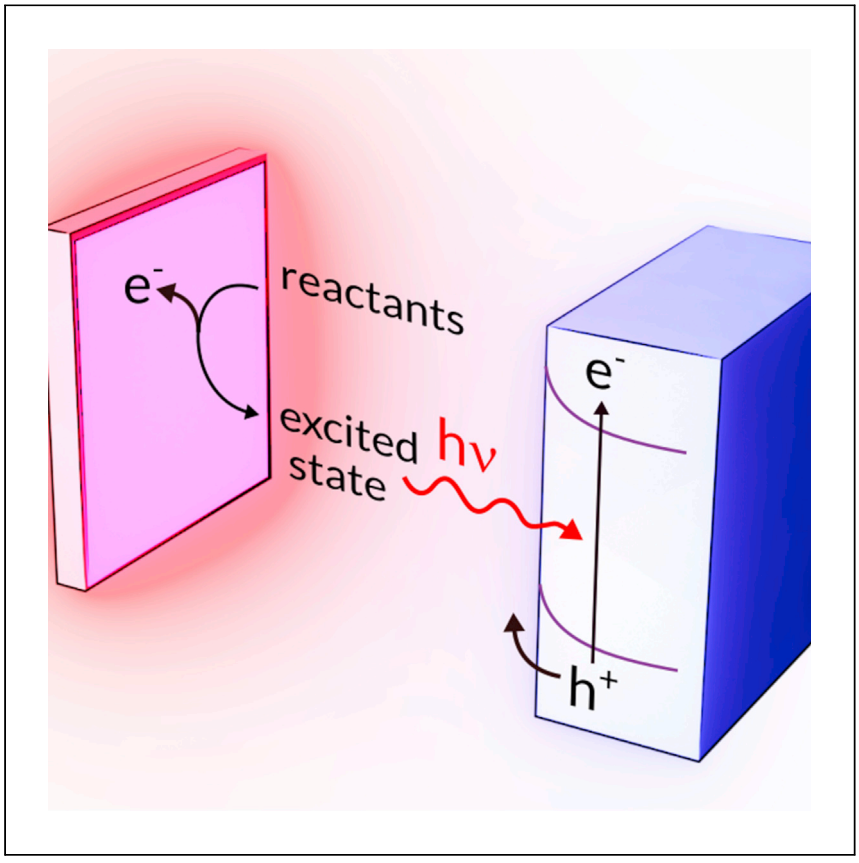

Semiconductor photoelectrochemistry is almost always induced and studied at surfaces illuminated with conventional light sources (solar simulator, LED, laser) located in the air outside the liquid phase. Zhao et al. report the possibility of inducing photoelectrochemistry using an electrochemical source of light, that is, the electrochemiluminescence emitted by a model co-reactant system.

Yiran Zhao, Jing Yu, Jean-François Bergamini, Yoan Léger, Neso Sojic, Gabriel Loget

neso.sojic@enscbp.fr (N.S.)
gabriel.loget@univ-rennes1.fr (G.L.)

Highlights

Electrochemiluminescence induces photoeffects at semiconductor/liquid junctions

Electrochemiluminescence-induced charge transfer can occur at such interfaces

Photovoltage and photocurrent variation is informative about distances or flow rates

Zhao et al., Cell Reports Physical Science 2, 100670
December 22, 2021
https://doi.org/10.1016/j.xcrp.2021.100670

Please cite this article in press as: Zhao et al., Photoelectrochemistry at semiconductor/liquid interfaces triggered by electrochemiluminescence, Cell Reports Physical Science (2021), https://doi.org/10.1016/j.xcrp.2021.100670

Cell Reports
Physical Science

Article

Photoelectrochemistry at semiconductor/liquid interfaces triggered by electrochemiluminescence

Yiran Zhao,[1] Jing Yu,[2] Jean-François Bergamini,[1] Yoan Léger,[4] Neso Sojic,[2,3,*] and Gabriel Loget[1,5,*]

SUMMARY

The photoelectrochemical charge-transfer process occurring at semiconductor surfaces has important implications in the fields of solar fuels and biodetection. Usually, physical light sources located outside the liquid phase, such as a solar simulator, a light-emitting diode (LED), or a laser, are used for photoelectrochemical studies. Here, we report inducing photoelectrochemistry using an electrochemical source of light, that is, the electrochemiluminescence (ECL) emitted by a model co-reactant system. Results reveal that the ECL illumination can activate several semiconductor (SC) photoelectrodes based on *n*-type Si, *n*-type GaAs, and *p*-type Si. We demonstrate that this emitter-receiver concept, based on dual-light conversion, enables photoelectrochemical charge transfer at the solid/liquid interface, which correlates with the ECL intensity. The singularities of this concept lie in the fact that light emission and collection both occur in the liquid phase, that ECL is an easily miniaturizable photon source, and that the SC/liquid junction can be easily implemented. This approach may open perspectives for remote ECL detection strategies and original photoelectrochemical analytical systems.

INTRODUCTION

Semiconductor (SC) photoelectrochemistry is a field of physical chemistry that is concerned with the interaction between a depleted SC and a liquid phase.[1,2] Upon illumination of the SC surface with photons of an energy higher than the SC bandgap (E_g), photogenerated minority carriers (holes [h^+] in the case of an *n*-type SC) are driven at the SC/liquid interface, creating a photovoltage (V_{oc}) in the depletion region. Typically, the V_{oc} is employed as an extra driving force for triggering redox reactions at reduced-input electrical energy. Promising applications of SC photoelectrochemistry are the conversion of solar energy into solar fuels[3–10] and the photoelectrochemical detection of molecular species.[11–15]

Another field of research that combines light and electrochemistry is electrochemiluminescence (ECL),[16–19] which is a very sensitive analytical technique widely used for bioassays. ECL intensity is proportional to the concentrations of the luminophore and the co-reactant.[19,20] Herein, the application of potential at a conducting electrode generates the excited state of a dissolved luminophore, which emits light when relaxing to its ground state. It is interesting to note that, in ECL, light is emitted at an electrode interface, and it can be considered as a light generator, whereas, in SC photoelectrochemistry, the electrode is a light absorber or receiver. These two phenomena have been merged in a few studies, leading to the concept of photoinduced electrochemiluminescence (PECL),[21–23] in which ECL is emitted at an illuminated SC photoelectrode. This concept has been explored using various SCs to

[1]Univ. Rennes, CNRS, ISCR (Institut des Sciences Chimiques de Rennes)-UMR6226, Rennes 35000, France

[2]University of Bordeaux, Bordeaux INP, ISM, UMR CNRS 5255, Pessac 33607, France

[3]Department of Chemistry, South Ural State University, Chelyabinsk 454080, Russian Federation

[4]Univ. Rennes, INSA Rennes, CNRS, Institut FOTON-UMR, 6082, Rennes 35000, France

[5]Lead contact

*Correspondence: neso.sojic@enscbp.fr (N.S.), gabriel.loget@univ-rennes1.fr (G.L.)

https://doi.org/10.1016/j.xcrp.2021.100670

create electrochemical systems allowing for emission at very low potentials,[24] Stokes and anti-Stokes light conversion,[23] localized emission,[25] and luminescence amplification.[26] SC photoelectrochemistry is almost always induced and studied at surfaces illuminated with conventional light sources, such as a solar simulator, a light-emitting diode (LED), or a laser located in the air outside the liquid phase. Therefore, the question is whether it would be possible to trigger SC photoelectrochemistry from a chemical light source, i.e., with solution-generated, excited states. In addition to being intriguing from a purely fundamental point of view with an emitter-receiver concept based on light conversion combined with redox reactions (i.e., electrogenerated light and photogenerated charge carriers), this could also be beneficial practically. First, the use of SC/liquid junctions could be useful for photon detection in the liquid phase with respect to conventional solid-state photodiodes because of their simple design based on an immersed SC as well as their cheap fabrication and implementation. In addition, using ECL as a light source may be beneficial because of the flexibility that it provides in terms of emission patterns, which are controlled by the electrode geometry. In addition, conventional monochromatic and polychromatic light sources have some disadvantages, such as their size, power consumption, excessive heat generation, as well as that they are designed to be used in air. Thus, photoelectrochemical detection triggered via illumination with solvated, excited molecules may open opportunities in the design of compact molecular-sensing devices.[11–15] In this regard, a few research reports have studied photocurrent generation at semiconducting assemblies of CdS quantum dots triggered by the chemiluminescence[27–29] and the ECL[30] of luminol analogs for biosensing applications.

In this article, we investigate the photogeneration of minority carriers at the surface of various *n*- and *p*-type photoelectrodes without a standard light source but via photons emitted during the concomitant electro-oxidation of tris(bipyridine)ruthenium(II) $[Ru(bpy)_3]^{2+}$ and tri-*n*-propylamine (TPrA) (Figure 1). This co-reactant model ECL system was chosen because (1) it is highly efficient and widely employed in commercial immunoassays and clinical diagnosis, and (2) ECL emission of this luminophore (620 nm, equivalent to 2 eV; lifetime of $[Ru(bpy)_3]^{2+*} \approx 0.6$ μs at room temperature in water)[31] is greater than the E_g value of several SCs.[19,32–34] Conceptually, this system presents some similarities with the electrochemical generator-collector configuration in which electrochemical information is transferred between two electrodes.[35–37] Our results show, for the first time, that photoelectrochemistry is possible with this system on properly selected SC surfaces.

RESULTS AND DISCUSSION

Description of the photoelectrochemical setup

Herein, we introduce an original photoelectrochemical design comprising an emitter/receiver dual-working-electrode (WE) system, depicted in the inset of Figure 1. In this configuration, photons of controlled energy (set by the selected luminophore) are generated through an anodic ECL reaction when an appropriate potential is applied to the emitter electrode. On the other side, a receiver electrode, composed of a depleted SC immersed into an electrolyte (in Figure 1, an *n*-type SC), is located in front of the emitter to absorb the electrogenerated light. If the energy of the produced photons is greater than the SC bandgap, minority carriers are expected to be generated (in Figure 1, the valence band holes $[h^+]$) and driven to the solid/liquid interface. In this out-of-equilibrium configuration, the energy of photogenerated carriers and that of the bulk SC are conceptually expressed by the quasi-Fermi-levels of the minority and the majority carriers, respectively. The V_{oc}, which is essentially the difference between the quasi-Fermi-level of minority carriers

Cell Reports
Physical Science
Article

CellPress
OPEN ACCESS

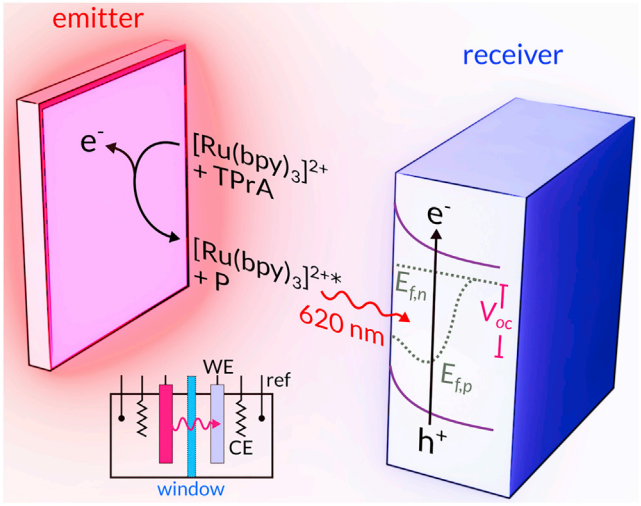

Figure 1. Photoelectrochemistry triggered by ECL

Scheme showing the operating principle of the emitter/receiver concept presented, based on dual-light conversion. An ECL reaction is triggered at the emitter electrode and generates a photovoltage (V_{oc}) at the receiver electrode (here, an *n*-type semiconductor). $E_{f,n}$ is the electron quasi-fermi level, and $E_{f,p}$ is the hole quasi-fermi level. Inset: Scheme depicting the cell that was used in this study. It comprises two electrochemical cells containing different electrolytes that are separated by a glass window.

($E_{f,p}$ in Figure 1) on the outermost part of the SC surface and that of the majority carriers ($E_{f,n}$ in Figure 1), can be measured experimentally.[1,38,39]

The emitter/receiver dual-WE system was designed, as shown schematically in Figure 1 (a detailed view of the cell is provided in Figure S1). We used a cell comprising two closed compartments in which are arranged two independent, three-electrode setups, which are individually addressed via a two-channel potentiostat. Each compartment comprises an Ag/AgCl reference electrode and a Pt counter electrode. The emitter compartment is filled with the ECL electrolyte (a pH-7.4-buffered solution containing 10 mM $[Ru(bpy)_3]^{2+}$ and 0.2 M TPrA) and a 1 cm^2 Pt-plate WE, which serves as the emitter. The ECL reagents are circulated to generate efficient convection in front of the emitter, ensuring intense and regular ECL emission at 620 nm. The second compartment contains a 0.1 cm^2 receiver SC WE immersed in an aqueous electrolyte. Both compartments are separated by a transparent glass window, which ensures hermeticity and optical transparency.

Individual characterizations of the emitter and receiver

Before studying the assembled dual-WE system, we characterized the emitter and the receiver components, separately. ECL emission at the surface of a Pt electrode was first characterized by performing cyclic voltammetry (CV) during recording of the ECL intensity using a photomultiplier tube (PMT). A phosphate-buffered saline (PBS) solution at pH 7.4 was selected because it is the optimal value to generate strong and stable ECL emission with the $[Ru(bpy)_3]^{2+}$/TPrA system.[20] This composition of the solution is classically used for bioassays because it provides strong ECL intensity.[20] The voltammetric and ECL plots, combined in Figure 2A, show that light emission (red curve) starts at a potential of ≈ 1 V (note that all the potential values in this article are referred versus Ag/AgCl, 3 M KCl) and increases until 1.25 V, well in line with the recorded current profile (black curve), which shows a strong anodic current wave in this range of potential. Depending on the experimental parameters

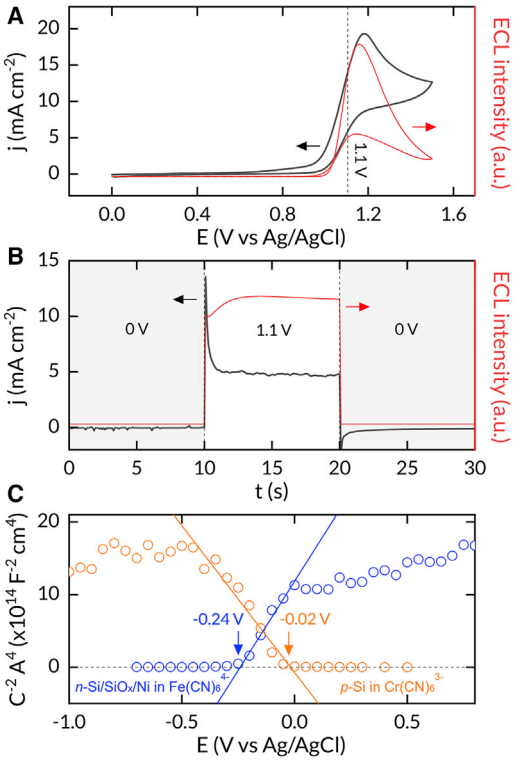

Figure 2. Characterization of the emitter and receiver

(A) Cyclic voltammogram (black curve) measured with a Pt electrode at a scan rate of 50 mV s^{-1}. Corresponding, normalized ECL intensity (red curve) measured with a photomultiplier tube placed in front of the electrode.

(B) Chronoamperogram (black curve) and normalized ECL intensity (red curve) measured with the Pt emitter electrode during sequential application of a potential E_{app} of 0 V and 1.1 V. The solution is composed of 10 mM $[Ru(bpy)_3]^{2+}$ and 0.2 M TPrA in phosphate buffer (pH = 7.4), and the electrolyte flow rate is 2.5 mL s^{-1}.

(C) Mott-Schottky (MS) analysis based on capacitance measurements recorded at 10 kHz for (blue) *n*-Si/SiO_x/Ni in a 1 M KCl solution containing 1 mM $Fe(CN)_6^{4-}$ and (orange) *p*-Si in a 1 M KCl solution containing in 1 mM $Cr(CN)_6^{3-}$. Circles are experimentally determined values, and lines are linear fits.

(electrode material, pH, concentration, surfactant, potential, etc.), several competitive mechanistic pathways may lead to the ECL emission of $[Ru(bpy)_3]^{2+}$ with TPrA co-reactant.[40–46] At Pt electrodes, the so-called "catalytic" route thus occurs predominantly (Figure S6).[40,41] Figure 2A shows that ECL emission occurs only at a potential in which $[Ru(bpy)_3]^{2+}$ is oxidized. Catalytic oxidation of TPrA by the electrogenerated $[Ru(bpy)_3]^{3+}$ occurs predominantly. This leads to the formation of the cation radical $TPrA^{\cdot+}$, which deprotonates to form the highly reducing neutral radical, $TPrA^{\cdot}$.[41,46] The excited state of $[Ru(bpy)_3]^{2+*}$ is obtained by the highly exergonic electron-transfer reaction between $TPrA^{\cdot}$ and $[Ru(bpy)_3]^{3+}$.[41,46] This later relaxes by emitting a photon at ≈620 nm. Figure 2B presents a typical chronoamperogram (CA; black curve) and the ECL intensity profile (red curve) measured during the application of a potential during 10-s-long steps of 0 V and 1.1 V. Figure 2B shows that ECL emission is instantaneously produced when the potential is switched on (E = 1.1 V) and immediately stopped when the potential is switched off (E = 0 V). Based on these data, in this article, ECL will be triggered through potentiostatic control at the Pt surface with an applied potential of 1.1 V to enable the emission ("ECL on") and 0 V to stop the emission ("ECL off") in the form of a squarewave potential signal.

Next, the SC/electrolyte junction of the receiver compartment was investigated. Although the use of several SCs will be discussed in this article, we focused this research on Si-based junctions for several reasons as follows: the ubiquity of Si in today's technologies,[47,48] its importance for photoelectrochemical research,[49,50] and its low bandgap (E_g = 1.1 eV), which allows absorption of photons of a wide energy range. The two doping types for Si were investigated. Although *p*-type Si (*p*-Si) photoelectrodes were employed directly after immersion in hydrofluoric acid (HF; which

Please cite this article in press as: Zhao et al., Photoelectrochemistry at semiconductor/liquid interfaces triggered by electrochemiluminescence, Cell Reports Physical Science (2021), https://doi.org/10.1016/j.xcrp.2021.100670

dissolves the native SiO_x layer and generates interfacial Si-H bonds), the *n*-type Si (*n*-Si) surfaces, which are particularly prone to electric passivation in anodic conditions,[51] were modified to ensure their photoelectrochemical stability. They were first chemically oxidized to form a ≈2-nm-thick SiO_x layer and, subsequently, coated with a 4-nm-thick Ni film deposited by magnetron sputtering (see Figure S2). These treatments allowed us to prepare metal-insulator-SC (MIS) *n*-Si/SiO_x/Ni photoanodes, which have been reported to be stable and efficient in drastic anodic conditions, such as that of water oxidation[52–54] and PECL.[23]

Photoanodes and photocathodes are typically employed to sustain oxidation and reduction reactions, respectively. Therefore, a specific redox species, i.e., a reductant—$K_4Fe^{II}(CN)_6$—or an oxidant—$K_3Cr^{III}(CN)_6$, optically transparent in the ECL emission range,[55,56] was added in the solution of the receiver compartment when the *n*-Si- and the *p*-Si-based photoelectrodes, were studied, respectively. A prerequisite that must be fulfilled to generate a V_{oc} at a photoelectrode is the formation of a suitable band bending in the SC (an upward band bending for an *n*-type SC is shown in Figure 1) and the establishment of an associated depletion region at equilibrium. The establishment of the depletion region in these conditions was experimentally investigated by dark capacitance measurements for each Si-based system. The results are shown as Mott-Schottky plots of Figure 2C, which allow for the determination of the flat band potential (E_{fb}).[1,2] The orange plot, which was recorded for *p*-Si in the $K_3Cr(CN)_6$ solution (measured pH = 7.9), shows that this junction exhibits an E_{fb} value of −0.02 V, which means that it is photoactive at lower potentials. Reciprocally, the blue plot reveals an E_{fb} value of −0.24 V for *n*-Si/SiO_x/Ni in the $K_4Fe(CN)_6$ solution (measured pH = 8.6); thus, this electrode is photoactive at higher potentials. The slopes of the linear fits (colored lines) were extracted and used to determine the free-carrier density (N_D). According to the Mott-Schottky relationship, N_D values of 2.97×10^{15} cm^{-3} and 2.45×10^{15} cm^{-3} were calculated for *p*-Si and for *n*-Si/SiO_x/Ni, respectively, which is in very good agreement with the range of resistivity (ρ) given by the manufacturer (1–5 Ω cm), attesting to the accuracy of our analysis.

Photovoltage measurements

Next, the emitter and receiver compartments were combined, as shown in the inset of Figure 1. Open circuit potential (E_{OCP}) measurements were performed at the receiver during switching the ECL emission of $[Ru(bpy)_3]^{2+}$/TPrA on and off at the emitter. Figure 3A reports a set of E_{OCP} values recorded as a function of time for various receiver electrodes when ECL is switched off (gray regions) and on (white region). Considering the Si-based electrodes that were described in Individual characterizations of the emitter and receiver. The orange curve shows that the dark E_{OCP} value for the *p*-Si is −0.7 V, which is more negative than the E_{fb} value determined in Figure 2C for this system (−0.02 V), confirming the presence of a depletion region at the *p*-Si interface during equilibrium. The slight variation in OCP is likely related to the evolution of the hydrogenated, unprotected Si surface with a composition that evolves during immersion time; however, that deviation is very slow and does not affect the nature of the junction. When at t = 10 s, ECL is switched on, the E_{OCP} switches to a value of −0.53 V, indicating a positive V_{oc} of +170 mV, as expected for a *p*-type photocathode under illumination.[1,57] A similar analysis can be drawn for *n*-Si/SiO_x/Ni, shown by the dark-blue curve in Figure 2. In the dark, its E_{OCP} value is 0.15 V, which is more positive than the E_{fb} is (−0.24 V), and when the ECL emission is switched on, the E_{OCP} decreases to a value of 0.08 V. In that case, a negative V_{oc} value of −72 mV is determined, which is also well in line with a *n*-type photoelectrochemical behavior.[1,57] The opposite signs of the determined V_{oc} for these two Si-based materials originate from the opposite band bending

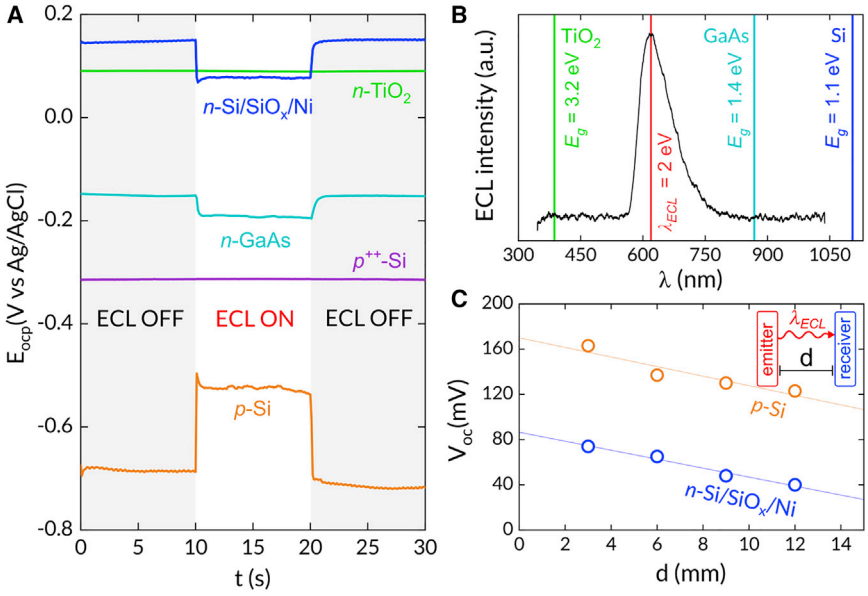

Figure 3. ECL-induced photovoltages

(A) OCP evolution as a function of time when the $[Ru(bpy)_3]^{2+}$/TPrA ECL is switched on and off for different semiconductor receivers located at d = 3 mm from the emitter. n-Si/SiO_x/Ni (dark blue), n-TiO_2 (green), and n-GaAs (light blue) were immersed in a 1 M KCl solution containing 1 mM $Fe(CN)_6^{4-}$, p^{++}-Si (purple) and p-Si (orange) were immersed in a 1 M KCl solution containing 1 mM $Cr(CN)_6^{3-}$.

(B) ECL emission spectrum of $[Ru(bpy)_3]^{2+}$/TPrA and bandgap positions for the semiconductors tested as receivers.

(C) Graph showing the photovoltage V_{oc} measured for p-Si in 1 mM $Cr(CN)_6^{3-}$ (orange circles) and n-Si/SiO_x/Ni in 1 mM $Fe(CN)_6^{4-}$ (blue circles) as a function of the distance d between the emitter and the receiver. Lines are linear fits of the experimental data. Inset: Scheme showing the distance d between the emitter and the receiver. The ECL electrolyte is composed of 10 mM $[Ru(bpy)_3]^{2+}$ and 0.2 M TPrA in phosphate buffer (pH = 7.4), and the electrolyte flow rate is 2.5 mL s^{-1}.

directions that promote accumulation of photogenerated minority carriers of opposite charge for each receiver under ECL illumination, i.e., e^- for the p-type receiver and h^+ for the n-type receiver. Measurements on a set of independently prepared electrodes led to average V_{oc} values of 159 ± 17 mV for p-Si and 68 ± 16 mV for n-Si/SiO_x/Ni photoelectrodes.

To provide additional evidence that ECL-based illumination can influence the energetics of SC photoelectrodes, we performed a negative control experiment by testing a degenerate Si-based electrode. This type of Si contains such a high density of free carriers that it has a quasi-metallic behavior. An HF-treated p^{++}-Si (ρ = 0.001–0.005 Ω cm) surface immersed in the $K_3Cr(CN)_6$ solution was used for that. In this case, as shown by the purple curve of Figure 3A, ECL emission did not affect its E_{OCP}. This behavior is exactly what was expected to occur because the free-carrier density in the p^{++}-Si is so high that photoactivity is inexistent. This series of results show clearly that a photovoltage can be produced by $[Ru(bpy)_3]^{2+}$/TPrA ECL on non-degenerate Si-based photoelectrodes.

Having explored the effect of doping, we decided to investigate the effect of the optical absorption of the receiver. For that, we employed the dual-WE system with moderately doped receivers (i.e., non-degenerate photoactive SC materials) having a bandgap different from that of Si. In this frame, n-type GaAs (n-GaAs), a direct-bandgap SC having a E_g value of 1.4 eV, in contact with the $K_4Fe(CN)_6$ solution,

was first employed. The influence of ECL emission on its E_{OCP} is shown by the light blue curve in Figure 3A. In this case, the ECL emission induced a negative E_{OCP} shift of V_{oc} (−40 mV), in good agreement with our previous observations for the *n*-Si-based photoanode. The smaller measured value compared with that of the *n*-Si/SiO_x/Ni photoanode can be attributed to charge recombination and/or energy level pinning occurring at the *n*-GaAs/liquid interface.[1,57] Conversely, an anatase *n*-type TiO_2 (*n*-TiO_2) electrode made by electrochemical anodization (see the Experimental procedures and Figure S3 for more details), which has a large, indirect bandgap (E_g = 3.2 eV), studied under the same conditions (green curve), did not exhibit any E_{OCP} variation, regardless of whether the ECL was switched on or off. These differences in photoelectrochemical behavior can be easily understood by comparing the energy of the photons emitted by the $[Ru(bpy)_3]^{2+}$/TPrA ECL and that of the SC bandgaps. These parameters are schematized in Figure 3B, which shows the ECL emission spectrum and indicates the bandgap energies of the SCs under scrutiny. Here, we can observe that most photons produced by the ECL process have an energy of 2 eV, which is higher than the Si and GaAs bandgaps, enabling light absorption in these materials. However, the bandgap of TiO_2 is too large for absorbing the emitted photons, which explains the independence of its E_{OCP} value as a function of the ECL emission and its absence of photoactivity in these conditions. Moreover, in another series of experiments, another ECL system, comprising luminol as a luminophore and H_2O_2 as a co-reactant in 0.1 M NaOH was employed in the emitter compartment. This ECL system is widely known and emits photons with a maximum intensity at 430 nm (Figure S4A).[58] Here, the three Si-based photoelectrodes previously employed were tested as receivers. As shown in Figures S4B and S4C, the V_{oc} results were essentially the same as those obtained with $[Ru(bpy)_3]^{2+}$/TPrA, highlighting the versatility of our concept.

Finally, the distance (*d*) between the emitter and the receiver was investigated for the two Si-based photoelectrodes with the $[Ru(bpy)_3]^{2+}$/TPrA ECL system. In these experiments, V_{oc} was measured when *d* varied from 3 to 12 mm, i.e., the emitter position was fixed 3 mm from the window, and the receiver position varied from 0 to 9 mm. The results, shown in Figure 3C reveal that, for both systems, V_{oc} decayed linearly as a function of *d* with a slope of ≈ 4 mV mm^{-1}. This phenomenon is caused by the divergent nature of ECL emission, which results in a decay of irradiance at the receiver surface when increasing the emitter-receiver distance. Indeed, if the ECL emitter is considered a Lambertian source, it has been shown that a variation of *d* in the order of the source size induces a significant decrease in the irradiance at the receiver surface,[59] which, in turn, decreases the V_{oc} value. If V_{oc} is expected to vary logarithmically over several decades of light intensity,[60,61] the remarkable linearity observed in both cases is not fully understood yet and likely originates from the irradiance variation as a function of *d* and the low range of light intensity produced in these experiments.

Photoelectrochemical charge transfer

To further investigate this dual system, we then studied the ECL-induced charge transfer at an SC receiver electrode. In these experiments, intermittent $[Ru(bpy)_3]^{2+}$/TPrA ECL was triggered by applying the previously described squarewave potential signal at 1 Hz, and the *n*-Si/SiO_x/Ni photoanode in the 1 mM $K_4Fe(CN)_6$ solution was used as a receiver.

The current density as a function of time for the emitter is shown in red in Figure 4A and its variation ensures that the anodic process corresponding to the ECL emission was intermittently generated, as previously discussed (see Figure 2B).

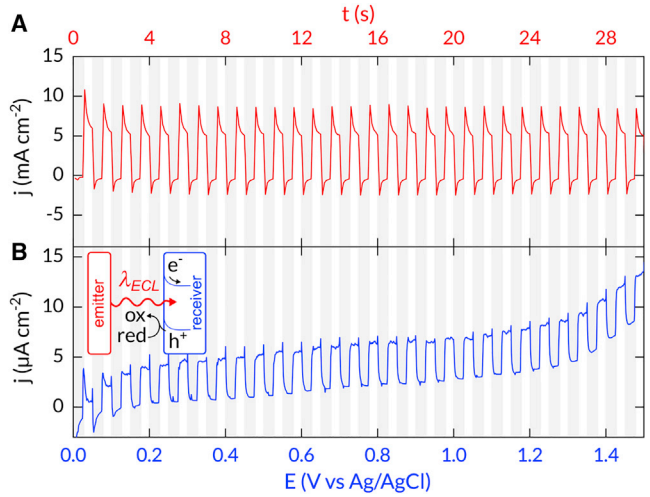

Figure 4. Interfacial transfer of minority carrier

(A) Chronoamperogram recorded at the emitter during the intermittent generation of $[Ru(bpy)_3]^{2+}$/TPrA ECL via the application of a 1-Hz squarewave signal comprising the steps of 0 V and 1.1 V. (B) Linear sweep voltammogram simultaneously recorded at the *n*-Si/SiO_x/Ni receiver placed at d = 3 mm from the emitter in a 1 M KCl solution containing 1 mM $Fe(CN)_6^{4-}$ at a scan rate of 50 mV s^{-1}. The ECL electrolyte is composed of 10 mM $[Ru(bpy)_3]^{2+}$ and 0.2 M TPrA in phosphate buffer (pH = 7.4), and the electrolyte flow rate is 2.5 mL s^{-1}.

Simultaneously, a synchronized potential sweep was applied to the receiver, the resulting current is presented in the voltammogram of Figure 4B. These voltammograms were stable and could be repeated several times when imposing successive cycles. Figure 4B shows that the ECL emission induces an increase in current at the receiver that is attributed to the interfacial charge transfer of photogenerated holes (depicted in the inset of Figure 4B). The photocurrent is instantaneously generated and stopped when ECL is switched on and off, respectively, and adds to the small dark current component. The photocurrent attributed to the oxidation of $Fe^{II}(CN)_6^{4-}$ to $Fe^{III}(CN)_6^{3-}$ and the shape of the voltammogram between 0 and 1.2 V (a photocurrent increase followed by a plateau) is in good agreement with a photoinduced charge-transfer process limited by the photogenerated charge carriers density. This makes sense when considering the order of magnitude of light intensity produced at the emitter. The photocurrent spikes observed at low potential are attributed to hole accumulation at the interface[62] and the dark current increase at high potentials to majority carrier tunneling through the interface for large band bending. From this curve, it can be deduced that a photocurrent density of ≈4 μA cm^{-2} is generated at the receiver in the light-limited regime. From this value, it is possible to qualitatively estimate the light intensity absorbed by the receiver considering an incident-photon-to-electron conversion efficiency (IPCE) of 70% for the photoelectrode at 620 nm. Note that the electrolyte in the receiver compartment is transparent to that wavelength,[55] and IPCE values comprised between 80% and 60% are typically determined by conventional photocurrent spectroscopy methods by our group[63] and others[64,65] for *n*-Si/Ni-based photoanodes. This photocurrent value would correspond to a light intensity value of ≈10 μW cm^{-2}. Although this value is qualitative, it points out the very low light intensity absorbed by the receiver, which is several orders of magnitude less than that measured in classical photoelectrochemical experiments, for instance, in solar water-splitting research typically performed with AM 1.5G solar simulators (100 mW cm^{-2}), light intensity is ≈10,000 times higher than in the present experiments. The effect of the emitter-receiver

distance *d* on the photocurrent was studied. As shown in Table S1, that parameter was found to affect the charge transfer at the receiver electrode considerably.

After showing that charge transfer can be triggered and measured at the receiver electrode, we next investigated the effect of ECL intensity on charge transfer. A straightforward method that can be used to control ECL intensity in a precise manner is to vary the flow (*Q*) of the ECL electrolyte in the emitter compartment, which controls the mass transfer of the ECL reactants (luminophore and co-reactant) at the emitter surface. The dependency of the ECL intensity on *Q* was confirmed by spectroscopic measurements that are presented in Figure S5. Because of this effect, the intensity of the ECL emission can be considered as an indicator of the liquid flow. In these experiments, we used the same dual-WE system, and a 50 mHz squarewave potential signal was applied to the emitter for triggering ECL intermittently. In the following experiments, the setup is identical to the previous ones, except that the flow rate of the electrolyte (10 mM $[Ru(bpy)_3]^{2+}$, 0.2 M TPrA in phosphate buffer (pH = 7.4)) is varied. The receiver (*n*-Si/SiO_x/Ni in the 1 mM $K_4Fe(CN)_6$ solution) was biased at a potential of 0.8 V, which, according to the voltammogram of Figure 4B, corresponds to a potential region in which the photoinduced charge transfer occurs, and dark current is rather low. Before the experiment, several (5 to 10) on/off ECL cycles were applied at the emitter in the quiescent electrolyte to reach a steady-state ECL profile for $Q = 0$ mL s^{-1}, and the current density was recorded at the emitter when *Q* was progressively increased up to 3.3 mL s^{-1} (Figure 5A). As shown in the CA of Figure 5C, the dark current remained the same and the photocurrent increased with *Q*. The photocurrent j_{ph}, plotted against the *Q* in Figure 5B, changes from 0.4 μA cm^{-2} for a quiescent electrolyte to 3.3 μA cm^{-2} for an electrolyte flow at 3.3 mL s^{-1}, which is a direct effect of the increase in ECL intensity. For flowing electrolytes, a sudden increase and decay in photocurrent was observed when switching on the ECL (Figure 5C). The origin of this behavior is yet unclear but may be explained by a transient ECL profile and/or charge accumulation at the photoelectrode/electrolyte interface.[62] This decay is responsible for the relatively large error bar (=2 SD) in Figure 5B (thin error bars). However, taking into account the steady-state photocurrent (recorded 2 s after switching on ECL) allows the error to be considerably reduced, as shown by the thick error bars in Figure 5B. These data show that ECL-induced charge transfer at an SC-based photoelectrode can be used for monitoring electrolyte flow in the emitter compartment.

To conclude, we have developed a dual-WE system composed of a metal ECL emitter and an SC-based photoelectrode receiver. This original design was employed to study the effects of ECL illumination on the photoelectrochemical behavior of the SC surface. It allowed us to demonstrate that photoelectrochemistry can be triggered at several SC/liquid photoactive junctions by ECL emission with the $[Ru(bpy)_3]^{2+}$/TPrA system. We have shown that ECL triggers negative and positive photovoltage at depleted *n*-type and *p*-type SC junctions, respectively, when the SC bandgap energy is less than that of the photons produced by the ECL reaction. In addition, our results demonstrate that ECL-induced charge transfer can occur at the SC/liquid interface. The associated variation in photovoltages and photocurrent can be used to determine simple physical parameters such as the distance between the emitter and the receiver as well as the electrolyte flow in the emitter compartment. This research strongly contrasts with conventional photoelectrochemistry works in which photons are emitted with a physical light source, such as a laser or an arc lamp. Although inherently limited by low emission intensity, this system brings significant advances that can be useful for analysis. The main points of this concept are the following: (1) light emission and collection are both realized in the liquid

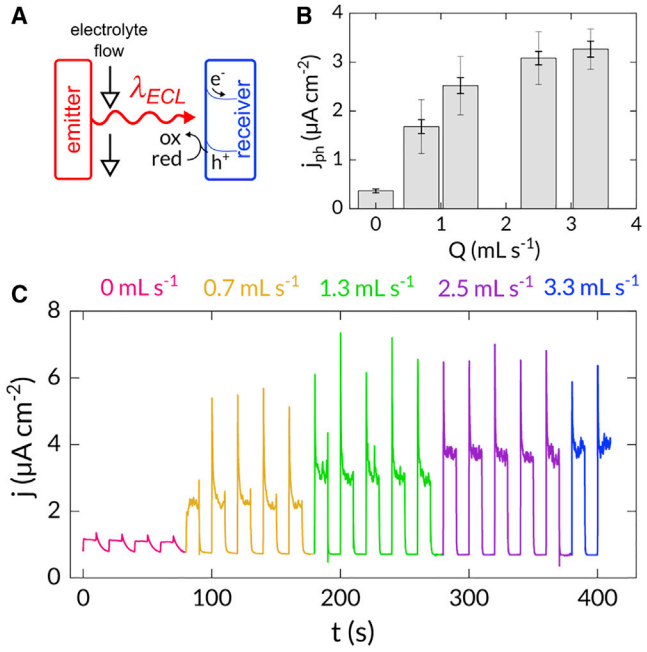

Figure 5. Flow rate measurements

(A) Scheme depicting experiments performed with a varying flow.

(B) Graph showing the evolution of the photocurrent as a function of the electrolyte flow. Error bars correspond to 2 SD. The thin error bars were calculated using the entire j_{ph} values, measured with ECL on. Thick error bars were calculated with j_{ph} values obtained 2 s after ECL was switched on.

(C) Chronoamperogram recorded at a *n*-Si/SiO_x/Ni photoanode in a 1 M KCl solution containing 1 mM $Fe(CN)_6^{4-}$ when $[Ru(bpy)_3]^{2+}$/TPrA ECL is switched on and off (by applying a 50 mHz squarewave signal at the emitter comprising steps 0 V and 1.1 V), and the ECL electrolyte is circulated at increasing flow rates: 0 (pink), 0.7 (yellow), 1.3 (green), 2.5 (purple), and 3.3 (blue) mL s^{-1}.The ECL electrolyte is composed of 10 mM $[Ru(bpy)_3]^{2+}$ and 0.2 M TPrA in phosphate buffer (pH = 7.4). *d* = 3 mm, and the applied potential is 0.8 V.

phase, (2) ECL is a photon source that can be easily miniaturized and precisely controlled,[66] and (3) the SC/liquid "receiver" junction can be easily implemented and miniaturized. Based on this, we think that this concept may find future applications for analytical applications.

EXPERIMENTAL PROCEDURES

Resource availability

Lead contacts

Further information and requests for resources should be directed to and will be fulfilled by the lead contact, Gabriel Loget (gabriel.loget@univ-rennes1.fr).

Materials availability

This study did not generate new unique reagents.

Data and code availability

All data are provided in the article and Supplemental information or are available for the corresponding authors upon request. This study did not generate any unpublished custom code.

Reagents

Acetone (MOS electronic grade, Erbatron, Carlo Erba Reagents) and anhydrous ethanol (RSE electronic grade, Erbatron. Carlo Erba Reagents) were used without

further purification. The ultrapure water had a resistivity of 18.2 MΩ cm (Purelab Classic UV). Sulfuric acid (96%, very large-scale integration [VLSI] grade. Selectipur) and hydrogen peroxide (30%, VLSI, Sigma-Aldrich) were purchased from BASF and Sigma Aldrich, respectively. Tris(bipyridine)ruthenium(II) chloride ($Ru(bpy)_3Cl_2$), tri-n-tripropylamine (TPrA) were purchased from Sigma-Aldrich. Phosphate-buffered saline solution (PBS, 100 mM, pH 7.3) was prepared from sodium phosphate dibasic heptahydrate and sodium phosphate monobasic monohydrate that were purchased from Sigma-Aldrich. $K_4Fe(CN)_6$ (≥99.95%) and $K_3Cr(CN)_6$ (99.99%) were purchased from Sigma-Aldrich.

Surface preparation

All vials and tweezers used for cleaning silicon were previously decontaminated in 3/1 v/v concentrated H_2SO_4/30% H_2O_2 at 105°C for 30 min, followed by copious rinsing with ultrapure water. Caution: the concentrated aqueous H_2SO_4/H_2O_2 (piranha) solution is very dangerous, particularly in contact with organic materials and should be handled extremely carefully. The *n*-type silicon wafers (1–5 Ω cm resistivity, phosphorus-doped, double-side polished, 280 μm) (100) were purchased from University Wafer, *p*-type silicon wafers (1–5 Ω cm resistivity, boron-doped, single-side polished, 275–325 μm) (100) were purchased from Siltronix, and p^{++}-type silicon wafers (0.001–0.005 Ω cm resistivity, boron-doped, single side polished, 490–510 μm) (100) were purchased from University Wafers. *n*-type GaAs (carrier concentration = 1–5 × 10^{18} cm^{-3}, silicon-doped, single-side polished, 325–375 μm) (100) was purchased from Wafer Technology. TiO_2 surfaces were composed of arrays of TiO_2 nanotubes (NTs) (Figure S3) that were prepared by anodization of Ti plates (Advent Research) at 90 V in an ethylene glycol solution containing 4.7 wt% water and 0.3 wt% NH_4F, followed by annealing at 500°C in the air to generate the anatase phase (as determined by X-ray diffraction). All the Si surfaces were degreased by sonication in acetone, ethanol, and ultrapure water for 10 min, respectively. The Si surfaces were then decontaminated and oxidized in piranha solution at 105°C for 30 min, followed by rinsing with copious amounts of ultrapure water and dried under an Ar flow. The Ni thin films were deposited on the clean *n*-Si/SiO_x surfaces by sputtering with a Leica EM ACE600 coating system (Ni target purity: 99.8%). The Ar pressure for sputtering was 2 × 10^{-2} mbar, and the current was 100 mA (pre-sputtering time of 1 min). The thickness of the film was determined *in situ* by a quartz crystal microbalance and measured by atomic force microscopy (Figure S2). After deposition, the system was degassed with N_2.

Electrode fabrication

Emitter electrode

A 1 cm^2 platinum plate connected to a metal wire was used as an emitter electrode. The back of the Pt plate was covered with hydrophobic tape.

Receiver electrodes

The coated surfaces and cleaned surfaces were further processed to fabricate the receiver electrodes. The ohmic contact was done on the backside of an Si wafer by scratching the surface with a diamond glass cutter; then, a droplet of InGa eutectic and a metal wire were applied on the scratched part. A thin layer of silver paste was painted to cover the InGa eutectic contact as well as a part of the metal wire. After the paste dried, epoxy resin (Loctite 9460, Henkel) was deposited to shield the backside and frontside of the surface, except for an active area of around 0.1 cm^2. The exact geometrical value was precisely measured using ImageJ software before the photoelectrochemical experiments. The electrodes were baked in the oven at 90°C for 1.5 h to cure the epoxy resin. Before their use in electrochemical

experiments, the unmodified Si electrodes (*p*-Si and p^{++}-Si) were dipped for 2 min in diluted HF (10%).

Electrochemical experiments

For the experiments of Figure 2A, voltammetric and ECL signals were recorded with a PGSTAT30 Autolab potentiostat connected to a conventional three-electrode cell, consisting of an Ag/AgCl/KCl 3M reference electrode, a Pt-wire auxiliary electrode, and a Pt working electrode. Before measurements, Pt electrodes were polished with alumina slurry of different size, rinsed thoroughly with Milli-Q water between each polishing step. ECL intensity was measured with a Hamamatsu photomultiplier tube (PMT) R5070A and a Hamamatsu C9525 high-voltage power supply. The PMT detector was held at −750 V and placed at a constant distance of 5 mm in front of the working electrode. The output signal was amplified with a Keithley 6485 Picoammeter before acquisition via the second input channel of the PGSTAT30 Autolab potentiostat.

CV, CA, electrochemical impedance spectroscopy (EIS), and OCP measurements were performed using a dual-channel potentiostat (SP 300, Biologic). The reference electrodes were Ag/AgCl, 3 M KCl for both emitter and receiver cells. The EIS measurements were performed in the dark with the Si-based electrodes as working electrodes, an amplitude of 10 mV, and a frequency of 10 kHz for a series of decreasing (*n*-Si/SiO_x/Ni) and increasing (*p*-Si) potential. An equivalent circuit comprising a resistor in parallel with a capacitance was used to obtain the capacitance of the space-charge layer. The description of the dual-WE device comprising two independent electrochemical cells is shown in Figure S1. The counter-electrode in the emitter compartment was a platinum ring and that of the receiver cell was a platinum rod. The emitter compartment was filled with the electrolyte that comprised 10 mM $[Ru(bpy)_3]^{2+}$, 0.2 M TPrA in the phosphate buffer solution with the pH adjusted to 7.4. This composition of the solution is classically used for bioassays because it provides strong ECL intensity.[20] The electrochemical experiments were performed in air-equilibrated solutions. The emitter working electrode had a surface of 1 cm^2, and the receiver working electrode had a surface of 0.1 cm^2. They were placed face to face in a parallel fashion and separated by a transparent glass window. The minimum distance between them was 3 mm. The emitter cell was connected to a peristaltic pump (Yanmis), allowing the electrolyte to flow from the bottom to the top. The ECL spectrum was recorded by a spectrometer connected to an optical fiber.

SUPPLEMENTAL INFORMATION

Supplemental information can be found online at https://doi.org/10.1016/j.xcrp.2021.100670.

ACKNOWLEDGMENTS

This work was funded by ANR (LiCORN, ANR-20-CE29-0006). J.Y. acknowledges the China Scholarship Council for her Ph.D. fellowship. The authors acknowledge Mekan Piriyev for providing the GaAs wafer. Dr. Lionel Santinacci is acknowledged for fruitful discussions.

AUTHOR CONTRIBUTIONS

Y.Z. and J.Y. performed the experiments. J.-F.B. designed the photoelectrochemical cell. Y.Z. and Y.L. analyzed the data. N.S. and G.L. conceived the idea, developed the methodology, and supervised the project. All authors wrote the manuscript.

DECLARATION OF INTERESTS

The authors declare no competing interests.

Received: August 18, 2021
Revised: October 1, 2021
Accepted: November 7, 2021
Published: December 1, 2021

REFERENCES

1. Memming, R. (2015). Semiconductor Electrochemistry (Wiley-VCH).
2. Tan, M.X., Laibinis, P.E., Nguyen, S.T., Kesselman, J.M., Stanton, C.E., and Lewis, N.S. (1994). Progress in Inorganic Chemistry, K.D. Karlin, ed. (Wiley-VCH), p. 21, 144.
3. Fujishima, A., and Honda, K. (1972). Electrochemical photolysis of water at a semiconductor electrode. Nature *238*, 37–38.
4. Bard, A.J. (1980). Photoelectrochemistry. Science *207*, 139–144.
5. Nocera, D.G. (2012). The artificial leaf. Acc. Chem. Res. *45*, 767–776.
6. van de Krol, R., and Grätzel, M. (2012). Photoelectrochemical hydrogen Production (Springer).
7. Montoya, J.H., Seitz, L.C., Chakthranont, P., Vojvodic, A., Jaramillo, T.F., and Nørskov, J.K. (2016). Materials for solar fuels and chemicals. Nat. Mater. *16*, 70–81.
8. Peter, L. (2021). Fundamental aspects of photoelectrochemical water splitting at semiconductor. Curr. Opin. Green Sustain. Chem. *31*, 100505.
9. Loget, G. (2019). Water oxidation with inhomogeneous metal-silicon interfaces. Curr. Opin. Colloid Interface Sci. *39*, 40–50.
10. Zhang, J., Cui, J., and Eslava, S. (2021). Oxygen evolution catalysts at transition metal oxide photoanodes: their differing roles for solar water splitting. Adv. Energy Mater. *11*, 2003111.
11. Willner, I., Patolsky, F., and Wasserman, J. (2001). Photoelectrochemistry with controlled DNA-cross-linked CdS nanoparticle arrays. Angew. Chem. Int. Ed. Engl. *40*, 1861–1864.
12. Devadoss, A., Sudhagar, P., Terashima, C., Nakata, K., and Fujishima, A. (2015). Photoelectrochemical biosensors: New insights into promising photoelectrodes and signal amplification strategies. J. Photochem. Photobiol. C Photochem. Rev. *24*, 43–63.
13. Zhao, W.W., Xu, J.J., and Chen, H.Y. (2015). Photoelectrochemical bioanalysis: the state of the art. Chem. Soc. Rev. *44*, 729–741.
14. Saada, H., Abdallah, R., Bergamini, J.F., Fryars, S., Dorcet, V., Joanny, L., Gouttefangeas, F., Olivier, S., and Loget, G. (2020). Photoelectrochemical sensing of hydrogen peroxide on hematite. ChemElectroChem *7*, 1155–1159.
15. Shu, J., and Tang, D. (2020). Recent advances in photoelectrochemical sensing: from engineered photoactive materials to sensing devices and detection modes. Anal. Chem. *92*, 363–377.
16. Liu, Z., Qi, W., and Xu, G. (2015). Recent advances in electrochemiluminescence. Chem. Soc. Rev. *44*, 3117–3142.
17. Hesari, M., and Ding, Z. (2015). Electrogenerated chemiluminescence: light years ahead. J. Electrochem. Soc. *163*, H3116–H3131.
18. Zhang, J., Arbault, S., Sojic, N., and Jiang, D. (2019). Electrochemiluminescence imaging for bioanalysis. Annu. Rev. Anal. Chem. (Palo Alto, Calif.) *12*, 275–295.
19. Sojic, N. (2020). Analytical Electrogenerated Chemiluminescence: From Fundamentals to Bioassays (The Royal Society of Chemistry).
20. Leland, J.K., and Powell, M.J. (1990). Electrogenerated chemiluminescence: An oxidative-reduction type ECL reaction sequence using tripropyl amine. J. Electrochem. Soc. *137*, 3127–3131.
21. Laser, D., and Bard, A.J. (1975). Semiconductor electrodes: Photo-induced electrogenerated chemiluminescence and up-conversion at semiconductor electrodes. Chem. Phys. Lett. *34*, 605–610.
22. Luttmer, J.D., and Bard, A.J. (1979). Electrogenerated Chemiluminescence: 34. Photo-induced electrogenerated chemiluminescence and up-conversion at semiconductor electrodes. J. Electrochem. Soc. *126*, 414–419.
23. Zhao, Y., Yu, J., Xu, G., Sojic, N., and Loget, G. (2019). Photoinduced electrochemiluminescence at silicon electrodes in water. J. Am. Chem. Soc. *141*, 13013–13016.
24. Yu, J., Saada, H., Abdallah, R., Loget, G., and Sojic, N. (2020). Luminescence amplification at $BiVO_4$ photoanodes by photoinduced electrochemiluminescence. Angew. Chem. Int. Ed. Engl. *59*, 15157–15160.
25. Vogel, Y.B., Darwish, N., and Ciampi, S. (2020). Spatiotemporal control of electrochemiluminescence guided by a visible light stimulus. Cell Reports Phys. Sci. *1*, 100107.
26. Yu, J., Saada, H., Sojic, N., and Loget, G. (2021). Photoinduced electrochemiluminescence at nanostructured hematite electrodes. Electrochim. Acta *381*, 138238.
27. Ding, C., Li, H., Li, X., and Zhang, S. (2010). A new strategy of photoelectrochemical analysis without an external light source based on isoluminol chemiluminescence probe. Chem. Commun. (Camb.) *46*, 7990–7992.
28. Tu, W., Wang, W., Lei, J., Deng, S., and Ju, H. (2012). Chemiluminescence excited photoelectrochemistry using graphene-quantum dots nanocomposite for biosensing. Chem. Commun. (Camb.) *48*, 6535–6537.
29. Ge, L., Wang, P., Ge, S., Li, N., Yu, J., Yan, M., and Huang, J. (2013). Photoelectrochemical lab-on-paper device based on an integrated paper supercapacitor and internal light source. Anal. Chem. *85*, 3961–3970.
30. Guo, Y., Sun, Y., and Zhang, S. (2011). Electrochemiluminescence induced photoelectrochemistry for sensing of the DNA based on DNA-linked CdS NPs superstructure with intercalator molecules. Chem. Commun. (Camb.) *47*, 1595–1597.
31. Van Houten, J., and Watts, R.J. (1976). Temperature dependence of the photophysical and photochemical properties of the tris (2, 2′-bipyridyl) ruthenium (II) ion in aqueous solution. J. Am. Chem. Soc. *98*, 4853–4858.
32. Zanut, A., Fiorani, A., Canola, S., Saito, T., Ziebart, N., Rapino, S., Rebeccani, S., Barbon, A., Irie, T., Josel, H.-P., et al. (2020). Insights into the mechanism of coreactant electrochemiluminescence facilitating enhanced bioanalytical performance. Nat. Commun. *11*, 2668.
33. Sentic, M., Arbault, S., Bouffier, L., Manojlovic, D., Kuhn, A., and Sojic, N. (2015). 3D electrogenerated chemiluminescence: from surface-confined reactions to bulk emission. Chem. Sci. (Camb.) *6*, 4433–4437.
34. Ma, C., Cao, Y., Gou, X., and Zhu, J.J. (2020). Recent progress in electrochemiluminescence sensing and imaging. Anal. Chem. *92*, 431–454.
35. Dengler, A.K., Wightman, R.M., and McCarty, G.S. (2015). Microfabricated collector-generator electrode sensor for measuring absolute pH and oxygen concentrations. Anal. Chem. *87*, 10556–10564.
36. Menshykau, D., O'Mahony, A.M., del Campo, F.J., Munõz, F.X., and Compton, R.G. (2009). Microarrays of ring-recessed disk electrodes in transient generator-collector mode: theory and experiment. Anal. Chem. *81*, 9372–9382.
37. Fosset, B., Amatore, C., Bartelt, J., and Wightman, R.M. (1991). Theory and experiment for the collector-generator triple-band electrode. Anal. Chem. *63*, 1403–1408.
38. Walter, M.G., Warren, E.L., McKone, J.R., Boettcher, S.W., Mi, Q., Santori, E.A., and

Lewis, N.S. (2010). Solar water splitting cells. Chem. Rev. *110*, 6446–6473.

39. Gerischer, H. (1979). Solar Energy Conversion: Solid-State Physics Aspects, B.O. Seraphin, ed. (Berlin: Springer), pp. 115–172.

40. Zu, Y., and Bard, A.J. (2001). Electrogenerated chemiluminescence, 67: Dependence of light emission of the tris(2,2′)bipyridylruthenium(II)/tripropylamine system on electrode surface hydrophobicity. Anal. Chem. *73*, 3960–3964.

41. Miao, W., Choi, J.P., and Bard, A.J. (2002). Electrogenerated chemiluminescence 69: the tris(2,2′-bipyridine)ruthenium(II), $(Ru(bpy)_3^{2+})$/tri-n-propylamine (TPrA) system revisited-a new route involving TPrA*+ cation radicals. J. Am. Chem. Soc. *124*, 14478–14485.

42. Valenti, G., Fiorani, A., Li, H., Sojic, N., and Paolucci, F. (2016). Essential role of electrode materials in electrochemiluminescence applications. ChemElectroChem *3*, 1990–1997.

43. Kanoufi, F., Zu, Y., and Bard, A.J. (2001). Homogeneous oxidation of trialkylamines by metal complexes and its impact on electrogenerated chemiluminescence in the trialkylamine/Ru $(bpy)_3^{2+}$ system. J. Phys. Chem. B *105*, 210–216.

44. Daviddi, E., Oleinick, A., Svir, I., Valenti, G., Paolucci, F., and Amatore, C. (2017). Theory and simulation for optimising electrogenerated chemiluminescence from tris (2,2′-bipyridine)-ruthenium (ii)-doped silica nanoparticles and tripropylamine. ChemElectroChem *4*, 1719–1730.

45. Guo, W., Zhou, P., Sun, L., Ding, H., and Su, B. (2021). Microtube electrodes for imaging the electrochemiluminescence layer and deciphering the reaction mechanism. Angew. Chem. Int. Ed. Engl. *60*, 2089–2093.

46. Zu, Y., and Bard, A.J. (2000). Electrogenerated chemiluminescence, 66: The role of direct coreactant oxidation in the ruthenium tris(2,2′) bipyridyl/tripropylamine system and the effect of halide ions on the emission intensity. Anal. Chem. *72*, 3223–3232.

47. Zhang, X.G. (2001). Electrochemistry of Silicon and Its Oxide (Kluwer Academic).

48. Lewis, N.S. (2016). Research opportunities to advance solar energy utilization. Science *351*, aad1920.

49. Sun, K., Shen, S., Liang, Y., Burrows, P.E., Mao, S.S., and Wang, D. (2014). Enabling silicon for solar-fuel production. Chem. Rev. *114*, 8662–8719.

50. Luo, Z., Wang, T., and Gong, J. (2019). Single-crystal silicon-based electrodes for unbiased solar water splitting: current status and prospects. Chem. Soc. Rev. *48*, 2158–2181.

51. Bae, D., Seger, B., Vesborg, P.C., Hansen, O., and Chorkendorff, I. (2017). Strategies for stable water splitting via protected photoelectrodes. Chem. Soc. Rev. *46*, 1933–1954.

52. Kenney, M.J., Gong, M., Li, Y., Wu, J.Z., Feng, J., Lanza, M., and Dai, H. (2013). High-performance silicon photoanodes passivated with ultrathin nickel films for water oxidation. Science *342*, 836–840.

53. Loget, G., Mériadec, C., Dorcet, V., Fabre, B., Vacher, A., Fryars, S., and Ababou-Girard, S. (2019). Tailoring the photoelectrochemistry of catalytic metal-insulator-semiconductor (MIS) photoanodes by a dissolution method. Nat. Commun. *10*, 3522.

54. Aroonratsameruang, P., Pattanasattayavong, P., Dorcet, V., Mériadec, C., Ababou-Girard, S., Fryars, S., and Loget, G. (2020). Structure–property relationships in redox-derivatized metal–insulator–semiconductor (MIS) photoanodes. J. Phys. Chem. C *124*, 25907–25916.

55. Frenzel, N., Hartley, J., and Frisch, G. (2017). Voltammetric and spectroscopic study of ferrocene and hexacyanoferrate and the suitability of their redox couples as internal standards in ionic liquids. Phys. Chem. Chem. Phys. *19*, 28841–28852.

56. Schaap, W.B., Krishnamurthy, R., Wakefield, D.K., and Coleman, W.F. (1969). Coordination Chemistry, S. Kirschner, ed. (Springer), pp. 177–206.

57. Chen, Z., Dinh, H.N., and Miller, E. (2013). Photoelectrochemical Water Splitting (Springer).

58. Miao, W. (2008). Electrogenerated chemiluminescence and its biorelated applications. Chem. Rev. *108*, 2506–2553.

59. Moreno, I. (2020). LED irradiance pattern at short distances. Appl. Opt. *59*, 190–195.

60. Kirchartz, T., Deledalle, F., Tuladhar, P.S., Durrant, J.R., and Nelson, J. (2013). On the differences between dark and light ideality factor in polymer: fullerene solar cells. J. Phys. Chem. Lett. *4*, 2371–2376.

61. Tress, W., Yavari, M., Domanski, K., Yadav, P., Niesen, B., Correa-Baena, J.P., Hagfeldt, A., and Graetzel, M. (2018). Interpretation and evolution of open-circuit voltage, recombination, ideality factor and subgap defect states during reversible light-soaking and irreversible degradation of perovskite solar cells. Energy Environ. Sci. *11*, 151–165.

62. Peter, L.M., Walker, A.B., Bein, T., Hufnagel, A.G., and Kondofersky, I. (2020). Interpretation of photocurrent transients at semiconductor electrodes: Effects of band-edge unpinning. J. Electroanal. Chem. (Lausanne) *872*, 114234.

63. Oh, K., Mériadec, C., Lassalle-Kaiser, B., Dorcet, V., Fabre, B., Ababou-Girard, S., Joanny, L., Gouttefangeas, F., and Loget, G. (2018). Elucidating the performance and unexpected stability of partially coated water-splitting silicon photoanodes. Energy Environ. Sci. *11*, 2590–2599.

64. Yu, X., Yang, P., Chen, S., Zhang, M., and Shi, G. (2017). NiFe alloy protected silicon photoanode for efficient water splitting. Adv. Energy Mater. *7*, 1601805.

65. Lee, S.A., Park, I.J., Yang, J.W., Park, J., Lee, T.H., Kim, C., Moon, J., Kim, J.Y., and Jang, H.W. (2020). Electrodeposited heterogeneous nickel-based catalysts on silicon for efficient sunlight-assisted water splitting. Cell Rep. Phys. Sci. *1*, 100219.

66. Zu, Y., Ding, Z., Zhou, J., Lee, Y., and Bard, A.J. (2001). Scanning optical microscopy with an electrogenerated chemiluminescent light source at a nanometer tip. Anal. Chem. *73*, 2153–2156.